Journal of
Materials Chemistry A

ROYAL SOCIETY OF CHEMISTRY

PAPER

Check for updates

Cite this: DOI: 10.1039/d5ta09457g

Tailoring high concentration electrolytes for supercapacitors: the impact of anion structure on ion transport and charge storage

Imgon Hwang,*[ab] Mantas Leketas,[ab] Ryan Bragg,[c] Sittipong Kaewmorakot,[ab] John M. Griffin[c] and Robert A. W. Dryfe*[ab]

Received 20th November 2025
Accepted 5th February 2026

DOI: 10.1039/d5ta09457g

rsc.li/materials-a

Electric double-layer capacitors (EDLCs) are promising energy storage devices due to their high power density and long cycle life, but their lower energy density compared to batteries remains a major limitation. Highly concentrated electrolytes present a safer and more sustainable alternative to conventional organic electrolytes, while retaining the ability to operate at high-voltage. Since many water-in-salt (WIS) electrolytes are based on fluorinated anions, the length of the fluorinated chain plays a critical role in determining electrolyte properties. In this study, we investigate the impact of anion structure by comparing three fluorinated imide-based salts, *i.e.* LiTFSI (lithium bis(trifluoromethanesulfonyl)imide), LiPFSI (lithium bis(pentafluoroethanesulfonyl)imide), and LiNFSI (lithium bis(nonafluorobutanesulfonyl)imide), for supercapacitor applications. Electrochemical characterization, Raman spectroscopy, and solid-state nuclear magnetic resonance (NMR) reveal that LiPFSI, with its higher proportion of double-donor single-acceptor (DDA) hydrogen bonding profiles, forms a highly coordinated anionic network at an optimal concentration of 5 mol kg^{-1}. Solid-state NMR spectroscopy shows that LiPFSI preferentially occupies the in-pore environment of nanoporous carbon, achieving a favourable ion to solvent balance that supports efficient charge storage and enhanced capacitance. In contrast, although LiNFSI can form dense ion agglomerates at high concentrations, the bulky anion and associated higher viscosity restrict ion transport and pore accessibility. These findings highlight the importance of anion selection and concentration, and pore-level electrolyte distribution in tailoring high-concentrated electrolytes for next-generation high-voltage, high-capacity supercapacitors.

1. Introduction

Electric double-layer capacitors (EDLCs) have attracted significant attention as energy storage devices that bridge the gap between electrolytic capacitors and rechargeable batteries in terms of energy and power performance.[1–4] While EDLCs offer higher power density than batteries, their lower energy density remains a challenge. To address this limitation, research has focused on developing high-capacity electrode materials and high-voltage non-aqueous electrolytes.[3,4] Organic electrolytes pose safety and environmental concerns, however, due to their toxicity, volatility, flammability, and low ionic conductivity.[5,6] As a safer and more sustainable alternative, aqueous electrolytes offer intrinsic stability, low cost, and high ionic conductivity, making them promising candidates for next-generation supercapacitors.[7–10]

An important recent development with aqueous electrolytes has been the development of highly concentrated water-in-salt (WIS) electrolytes, which significantly expanded the electrochemical stability window (ESW) towards 3 V, *i.e.* far exceeding the 1.23 V limit of conventional aqueous electrolytes.[11] This innovation, although reported in the context of Li$^+$-ion batteries, has been used to narrow the performance gap between aqueous and organic-based supercapacitors, making WIS electrolytes attractive for next-generation energy storage applications.[11–23] Among various electrolyte candidates, imide-based anions such as lithium bis(trifluoromethanesulfonyl) imide (LiTFSI) have demonstrated excellent thermal and electrochemical stability, in turn prompting research into their use in high-voltage aqueous supercapacitors.[11] These unique properties have driven extensive exploration of imide-based WIS electrolytes for high-voltage energy storage applications.[23–31] Despite the success of WIS electrolytes, most prior studies have focused on single salt systems at extremely high concentrations (typically >20 mol kg^{-1}, hereafter denoted m),[31] where water molecules are fully coordinated and free solvent is nearly absent. However, recent studies have revealed that many relevant physicochemical changes—such as ion pairing, clustering,

---

[a] *Department of Chemistry, University of Manchester, Oxford Road, Manchester, M13 9PL, UK. E-mail: imgon.hwang@manchester.ac.uk; robert.dryfe@manchester.ac.uk*

[b] *Henry Royce Institute, University of Manchester, Oxford Road, Manchester, M13 9PL, UK*

[c] *Department of Chemistry, Lancaster University, Lancaster, LA1 4YB, UK*

and non-ideal transport behavior—begin to manifest themselves at intermediate concentrations, well below the canonical WIS threshold.[32,33] For example, Suh *et al.* demonstrated that LiTFSI and $NaClO_4$ electrolytes reach maximum ionic conductivity near 5–6 m, with further increases in concentration leading to enhanced ion aggregation and reduced mobility due to stronger cation–anion interaction.[34] These findings suggest that the optimal properties of concentrated electrolytes may emerge in the 5 m regime, where conductivity is maximized, marking a transition where ion–ion interactions begin to dominate over ion–solvent interactions, even though water is still the majority component.[34]

This study introduces a comparative analysis of three fluorinated imide-based anions, LiTFSI, lithium bis(pentafluoroethanesulfonyl)imide (LiPFSI), and lithium bis(nonafluorobutanesulfonyl)imide (LiNFSI), to elucidate how variations in fluorinated chain length influence ion solvation, electrolyte–carbon interactions, and charge storage mechanisms. A combination of Raman spectroscopy and solid-state nuclear magnetic resonance (NMR) spectroscopy is employed to provide multi-scale understanding. Raman spectroscopy is used to investigate the solvation structure and hydrogen-bonding interactions in the electrolyte, providing insights into how different anions influence the local ionic environment,[35,36] while solid-state NMR offers molecular-level insights into electrolyte behavior within nanoporous carbon electrodes, clarifying anion-dependent ion accessibility and charge storage mechanisms.[37,38]

To the best of our knowledge, this is the first comparative study of LiTFSI, LiPFSI, and LiNFSI electrolytes at intermediate concentrations (~5 M), combining the methods mentioned above to link bulk solvation structure and pore-level ion partitioning with supercapacitor performance. Unlike prior work that predominantly focused on single salts at ultra-high concentrations, this work probes the structure–property relationships across different anions, integrating analysis from bulk electrolyte characterization to in-pore molecular behavior and device-level electrochemical performance. This approach provides insight into how molecular–scale interactions translate into ion transport, electrolyte partitioning, and charge storage efficiency, thereby informing the rational design of high energy density aqueous supercapacitors.

2. Experimental

2.1. Electrode preparation

YEC-8a activated carbon (Fuzhou Yihuan Carbon, China), C750 graphene nano-platelets (XGSciences, USA) and polytetrafluoroethylene (PTFE, 60 wt% dispersion, Sigma-Aldrich, UK) in an 8 : 1 : 1 mass ratio were dispersed in iso-propyl alcohol (IPA, Fisher Chemical, UK). The slurry was stirred for at least 2 hours until most of the solvent evaporated to achieve a non-sticky, mouldable consistency. The flattened film was rolled into 50 μm thick sheets using an Electric Cold Roller Press (model MSK-HRP-MR100DC MTI, KJ Group, USA). The sheets were dried in an oven at 70 °C for one hour, then transferred to a vacuum oven and dried overnight at 100 °C. Dried sheets were punched into discs of 12 mm diameter (approximately 7 mg). Electrodes using YP-50F carbon (Kuraray, Japan) were prepared following the same procedure.

The electrodes were prepared manually, and some variation in mass loading between samples is therefore unavoidable. Based on repeated electrode mass measurements, the mass loading variation was estimated to be within approximately ±20%, which is typical for manually prepared porous carbon electrodes. To minimize the influence of this variability, electrochemical measurements were consistently performed using material taken from the central region of the electrode coatings, where thickness and composition are most uniform.

2.2. Physical characterization

The shear viscosity of the electrolytes was measured using a Kinexus Pro+ rotational rheometer (Malvern Instruments Ltd, Worcestershire, UK). All measurements were conducted at a controlled temperature of 25.00 ± 0.01 °C. A fixed gap of 1 mm was set, and any excess sample was removed. A total of 1.09 mL of each sample was carefully loaded onto the measuring plate. Shear viscosity curves were acquired through a shear rate ramp ranging from $0.1\ s^{-1}$ to $100\ s^{-1}$. The ionic conductivity values were obtained using a conductivity meter (Seven Excellence with an Inlab 731 4-pole cell and pH electrode InLab Excert Pro-ISM, Mettler Toledo, Switzerland) at room temperature. The conductivity and viscosity measurements were repeated twice independently.

Raman spectra were acquired using a Renishaw inVia microscope equipped with a 532 nm excitation laser (Renishaw, UK), operating at a power of 0.274 mW, with a grating of 1800 lines per mm and a 50× long working distance objective. Deconvolution of the Raman spectra was carried out using a Gaussian function, allowing peak positions to vary freely to achieve the best fit with the experimental data. Deconvolution was performed with Microcal Origin 2022b (OriginLab Co., Northampton, MA, USA), applying 5-point Savitzky–Golay smoothing to determine the number and positions of sub-bands. Prior to analysis, the spectra were baseline-corrected. The bands were then deconvoluted into the most appropriate number of Gaussian components by monitoring both the residual sum of squares and the χ^2 value as functions of the number of Gaussian components.[39] X-ray diffraction (XRD) analysis was performed on free-standing activated carbon samples using a Philips X'pert PRO diffractometer with Cu Kα radiation ($\lambda = 0.154$ nm) and operating at 40 kV and 30 mA.

The wetting properties of the concentrated electrolyte were investigated using a Theta Optical Tensiometer (Biolin Scientific, Finland) with OneAttension software (version 2.3). In this experiment, the droplet size was controlled at a fixed volume of 1.5 μL. Measurements were performed statically in a humidity chamber to minimize liquid evaporation. A non-porous carbon substrate, the basal plane of highly ordered pyrolytic graphite (HOPG, ZYA grade, Scanwel, USA), was used as a proxy for the activated carbon material. Images were captured after the electrolyte was placed on the HOPG ($t = 30$ s) at a rate of 10.2 Hz. The contact angles were analyzed using OneAttension software, based on the Young–Laplace equation.[40,41] Contact angle measurements were performed with more than ten independent droplets for each electrolyte.

2.3. Electrochemical characterization

For 2-electrode symmetric coin cells, CR2032-type casings were used. The cells were assembled with free-standing nanoporous activated carbon (AC) electrodes as both the anode and cathode, a porous glass microfiber membrane (Whatman, thickness = 0.2 mm) as the separator, and 100 μL of electrolyte. LiTFSI (99%, Fluorochem), LiPFSI (98%, Tokyo Chemical Industry UK Ltd), and LiNFSI (95%, Tokyo Chemical Industry UK Ltd) at concentrations ranging from 1 m to 10 m with ultrapure distilled water (18.2 MΩ cm resistivity, Millipore Milli-Q, Merck). The coin cells were assembled using a hydraulic crimper (MSK-160D, MTI Corp.) under 0.9 tons applied weight.

The 3-electrode electrochemical investigations were performed in Poly(etheretherketone) (PEEK) Swagelok-type cells by sandwiching a porous glass microfiber membrane (Whatman, thickness = 0.20 mm) between two electrodes and graphite foil current collectors. For the electrolyte stability investigations, three-electrode cells were built with a working AC electrode (~7 mg), a greater mass of AC (~30 mg) as a counter electrode and a silver-wire pseudo-reference electrode (AgQRE[37,42]). The AgQRE was calibrated using a standard redox couple (10 mM ferrocene solution in an ionic liquid), and its stability was verified subsequently by monitoring the open-circuit potential directly in the corresponding electrolytes over the duration of the electrochemical measurements. All the cells were filled with the 1, 5 or 10 m LiTFSI, LiPFSI, or LiNFSI electrolyte solutions. The electrochemical measurements in three-electrode cells were conducted by cyclic voltammetry (CV) at 1, 10, and 100 mV s^{-1} and the galvanostatic charge and discharge (GCD) method at 1, 2, 5, 10 A g^{-1} with the working electrode swept between 0 and +0.5 V (positively) and 0 and −0.5 V (negatively) *vs.* the Ag wire quasi-reference electrode. Electrochemical impedance spectroscopy (EIS) measurements were performed at 0 V (two-electrode configuration) and at 0 V (*vs.* AgQRE, three-electrode configuration), using a 5 mV amplitude ac modulation across a frequency range of 100 kHz to 10 mHz.

All electrochemical measurements (CV, GCD, and EIS) were performed using independently prepared electrodes and electrolyte batches, showing good reproducibility (variation ±5%). Electrochemical performance is reported as gravimetric capacitance (F g^{-1}) to account for any minor variations in electrode mass.

2.4. Nuclear magnetic resonance

NMR measurements were performed using a 400 MHz Bruker Avance III HD WB spectrometer operating at a magnetic field strength of 9.4 T. YEC-8a powder (13 mg) was packed into 3.2 mm outer-diameter zirconia rotors and electrolyte solutions (22.5 μL) were injected with a microsyringe. The magic-angle spinning (MAS) rate was 5 kHz. For each sample the recycle interval was set to at least $5 \times T_1$ (as measured by a saturation recovery experiment) and the 90° pulse length was optimized for each sample to ensure that spectra were recorded under quantitative conditions. All NMR spectra were deconvoluted using the DMfit program[43] to yield integrated resonance intensities with a Gaussian-to-Lorentzian ratio between 0 and 1. All spectra were well fitted with a single peak for the in-pore resonance and a single peak for the ex-pore resonance.

3. Results and discussion

We investigated the physical properties of three electrolyte solutions (LiTFSI, LiPFSI, and LiNFSI) by analyzing their ion conductivity and viscosity at concentrations of 1 m, 5 m, and 10 m. As expected, ionic conductivity decreased with increasing anion size, reflecting the reduced mobility associated with longer fluorinated chains and stronger ion–ion interactions[44] (Fig. S1). Such behavior is consistent with experimental viscosity due to enhanced intermolecular interactions and chain entanglement.[44] For all three electrolytes, conductivity reaches a maximum at intermediate concentrations (around 5–7 m) and decreases at higher concentrations as ion–ion interactions intensify and water activity is reduced (Fig. S2). The largest anion, $NFSI^-$, exhibits a stronger tendency toward ion pairing and aggregation, which increasingly limits charge-carrier mobility as concentration rises. While viscosity increases with anion size at low concentrations, LiNFSI shows a markedly higher viscosity at 10 m compared to LiTFSI and LiPFSI (Fig. S1b). This indicates the formation of more rigid, interconnected ionic networks under highly concentrated conditions, where strong anion–cation correlations and aggregation dominate the solution structure. The concurrent increase in viscosity and decrease in conductivity for LiNFSI thus originate from the same underlying effect, namely the size and strongly associating nature of the $NFSI^-$ anion, which promotes aggregation and hinders ion transport at high concentrations.

As well as bulk interactions, understanding of capacitance requires some knowledge of electrolyte–substrate interactions, hence the wettability of the electrolytes on highly ordered pyrolytic graphite (HOPG) was evaluated using contact angle measurements shown in Fig. S3. At a concentration of 5 m for each electrolyte, the solution contact angles in air were approximately 23(±2.8)° for LiTFSI, 24(±3.6)° for LiPFSI, and 18(±5.3)° for LiNFSI. These values are significantly lower than those of pure water on HOPG (62°),[45] reflecting the affinity of the fluorinated anion for the graphite surface. LiNFSI shows the lowest contact angle: increased wettability is significant because it reflects stronger adsorption of the electrolyte on the electrode, which can increase ion accessibility and improve electrochemical properties at the electrode–electrolyte interface.

To achieve deeper insights into how the fluorinated anions affect the conductivity and electrochemical behavior of the electrolytes, we employed Raman spectroscopy to probe the chemical environment of water molecules in the electrolytes. Fig. 1 shows the OH stretching modes of LiTFSI, LiPFSI, and LiNFSI aqueous solutions at concentrations of 1 m, 5 m, and 10 m. The broad Raman band was deconvoluted into three Gaussian peaks corresponding to double-donor double-

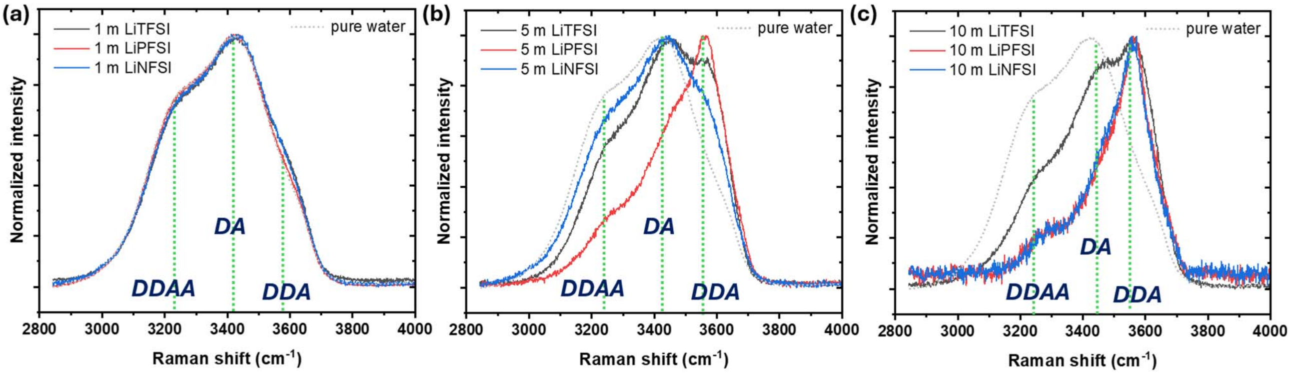

Fig. 1 Raman OH stretching vibration of LiTFSI, LiPFSI, and LiNFSI at the (a) 1 m, (b) 5 m, and (c) 10 m concentrations.

acceptor (DDAA), double-donor single-acceptor (DDA), and single-donor single-acceptor (DA) hydrogen bonding motifs. The deconvolution procedure and representative fitting results for the OH stretching region are provided in Fig. S4 and Table S1. This approach is commonly used to analyze changes in hydrogen-bonding networks that arise from variations in electrolyte composition and concentration.[46,47]

At a concentration of 1 m, the Raman spectra of all three electrolytes exhibit similar OH vibration characteristics that closely resemble those of pure water (Fig. 1a). This similarity suggests that at low concentrations, the solvation structures of the electrolytes are largely comparable, with lithium cations (Li^+) being well-solvated by water molecules and the anions ($TFSI^-$, $PFSI^-$, $NFSI^-$) remaining largely dissociated in solutions. As the concentration increases to 5 m, distinct differences in solvation and ion association begin to emerge. Deconvolution of the OH stretching region reveals that the proportion of strongly hydrogen-bonded water molecules (DDAA structures) varies among the electrolytes in the order LiNFSI > LiTFSI > LiPFSI, while the content of moderately hydrogen-bonded species (DDA structures) follows the reverse trend (Fig. 1b). These variations reflect how each anion modulates the local solvation environment, indicating that the identity of the anion plays a critical role in determining the balance between free and associated Li^+ species. This evolving solvation behaviour suggests that, at intermediate concentrations, anion-dependent ion association plays a dominant role in shaping electrolyte structure. In the case of LiPFSI, the lower DDAA and higher DDA content imply the formation of a more compact and aggregated anionic network,[48] which likely limits the availability of free, fully solvated Li^+ ions.[49] Conversely, the higher DDAA content observed for LiNFSI indicates the presence of a larger fraction of bulk-like water molecules that are less directly involved in Li^+ solvation. This behavior is consistent with stronger ion–ion interactions and the formation of contact ion pairs or aggregates, which reduce the availability of water molecules for cation coordination. LiTFSI exhibits intermediate characteristics, reflecting a balance between ion dissociation and aggregation arising from the competing effect of charge delocalization and coordination flexibility of the $TFSI^-$ anion. Together, these distinctions highlight a progressive evolution of solvation with concentration, driven by enhanced ion–ion interactions and reduced effective solvation of Li^+.

Additional insight into these interactions is provided by Raman spectra of LiNFSI in aqueous solution, which reveal a concentration-independent S–N–S stretching mode centred at approximately 732 cm^{-1} across the full investigated concentration range (1–10 m, see Fig. S5). This spectral invariance suggests a stable solvation structure for the $NFSI^-$ anion and indicates that increasing salt concentration does not significantly perturb its local coordination environment. Notably, a distinct shoulder at ~752 cm^{-1} persists across all concentrations, including the most dilute regimes (normalized Raman spectra as shown in Fig. S5d). The persistence of this higher-frequency feature under dilute conditions rules out its origin being due to bulk aggregation or concentration-induced clustering. Instead, its spectral position and stability suggest the presence of contact ion pairs (CIP) or chelated Li^+–$NFSI^-$ complexes, coexisting alongside more weakly bound or solvent-separated species.[50,51] Similar shoulders have been identified in other aqueous salt systems, where they have been conclusively assigned to strongly coordinated contact ion pairs, observable even at low concentrations.[50,51] This behaviour stands in marked contrast to that observed for the structurally related LiTFSI and LiPFSI salts. In those systems, the S–N–S stretching mode typically appears near ~740–745 cm^{-1}, but exhibits a progressive blue shift (toward higher frequencies) as salt concentration increases. This shift has been widely interpreted as a spectroscopic signature of increasing Li^+–anion interaction strength, caused by the formation of contact ion pairs and higher-order aggregates (*e.g.*, triple ions or clusters) due to reduced solvent availability and enhanced electrostatic correlation at higher concentrations.[52] Namely, in contrast to LiTFSI and LiPFSI, where increased concentration induces stronger pairing, LiNFSI appears to form stable CIPs even in dilute solutions, contributing to persistent transport limitations across the full concentration range. Notably, the presence of stable contact ion pairs in LiNFSI even at low concentration, as suggested by Raman analysis, provides a potential microscopic explanation for its higher viscosity and lower ionic conductivity. Persistent ion pairing and aggregation increase the effective hydrodynamic size of charge carriers and reduce the population of free Li^+ ions, thereby simultaneously enhancing viscous resistance and suppressing ionic mobility, consistent with molecular dynamics and scattering studies of imide-based water-in-salt electrolytes.[48]

These differences in solvation structures across concentrations highlight distinct trends in ion pairing, aggregation, and water interactions, all of which are crucial determinants of electrolyte performance in energy storage applications.[48] The unique behavior of LiPFSI, characterized by a higher DDA content at 5 m, is indicative of a moderately structured hydrogen-bonding network that promotes enhanced ion transport and improved pore accessibility (*vide infra*). Conversely, LiNFSI, with its larger anion size and comparatively weaker hydrogen-bonding networks, exhibits more pronounced transport limitations at higher concentrations due to its solvation dynamics and ion aggregation behavior.

To experimentally assess the electrochemical performance of high-concentration electrolytes containing different anionic species, symmetric two-electrode coin cells were assembled and evaluated using cyclic voltammetry (CV) and galvanostatic charge–discharge (GCD) techniques. The electrodes were fabricated from commercially available activated carbon (YEC-8A), featuring a surface area of 2390 $m^2\ g^{-1}$ and a pore size distribution with a peak maximum at approximately 0.87 nm.[37] As shown in Fig. S6, the CVs obtained at a scan rate of 10 $mV\ s^{-1}$ reveal that all three electrolytes achieve maximum capacitance near 5 m concentration: the capacitance values are presented in Fig. S7a. At higher scan rates, the current response is increasingly dominated by surface-controlled capacitance, thereby minimizing differences in overall capacitance due to reduced diffusion effects.[53,54] Under these conditions, the capacitance largely reflects the electrolyte's ability to support rapid ion transport—a behaviour consistent with the observed ion conductivity and viscosity trends (Fig. S1 and S2). The CV responses shown in Fig. 2a–c, recorded at a scan rate of 1 $mV\ s^{-1}$, reveal that pore transport effects become increasingly important, leading to more pronounced differences in capacitance across the electrolytes (Fig. S7b).[54] Under these slow conditions, sufficient time is available for ions to penetrate the nanoporous carbon electrode, making diffusion-controlled capacitance within the pores the dominant charge storage mechanism.[37] At this scan rate, LiTFSI and LiPFSI exhibit comparable capacitance values (Fig. S7b). Similarly, contact angle measurements on HOPG suggest nearly identical wettability between these electrolytes (see discussion above and Fig. S3). In contrast, LiNFSI displays significantly lower capacitance at 1 $mV\ s^{-1}$. Interestingly, it also shows the lowest contact angle (18(±5.3)° at 5 m), indicating high apparent surface wettability on HOPG: this reflects the trade-off between the higher adsorption of the NFSI and reduced pore accessibility because of its larger size/lower viscosity. Note that the differences between the idealized (planar, basal plane HOPG) and capacitive electrode (activated carbon, mixed with binder and graphene) materials makes direct comparison difficult. We emphasis the notable reduction in contact angle relative to pure water (62°)[45] – highlighting the substantial enhancement in wetting behavior induced by the presence of these salts. This observation is particularly important because good wetting is a prerequisite for electrolyte access to nanoscale pores. This behavior is consistent with porous electrode theories, which suggests that during longer charge times, ions first occupy larger interparticle voids before diffusing into smaller pores.[55]

Capacitance values derived from GCD measurements (Fig. 2d–f and S8–S10) align well with the CV results, reaffirming that peak capacitance is achieved at a concentration of 5 m. This consistency across techniques suggests that the high bulk ionic conductivity observed at 5 m (Fig. S1b) effectively translates to efficient in-pore ion transport, supporting enhanced charge storage. In other words, the favourable bulk transport properties at this concentration appear to facilitate ion access into the porous electrode structure, enabling maximum utilization of the available surface area. This correlation highlights the importance of optimizing not just ionic concentration, but also the interplay between ion mobility and pore accessibility. At 1 m and 5 m, capacitance increases with the applied voltage window, potentially due to enhanced charge storage and minor contributions from faradaic side reactions, such as electrode oxidation. However, at 10 m, this trend plateaus despite the higher ionic concentration, likely due to increased viscosity and reduced mobility, which hinder further charge accumulation. Although both CV and GCD characterize charge storage, they do so under different control modes. CV, being a potentiostatic technique, allows rapid evaluation of surface and diffusion-controlled processes across a range of time scales, depending on the scan rate. In contrast, GCD, being galvanostatic in nature, subjects the system to a constant current, revealing how the electrolyte responds to sustained ion flow and longer charge duration. These complementary approaches offer a more comprehensive understanding of the underlying electrochemical mechanisms.[56] Finally, while higher voltage windows can improve capacitance, they also increase the risk of electrolyte decomposition or carbon oxidation, especially in more dilute electrolytes, *e.g.* the 1 m solution. Raman spectroscopy (Fig. 1) indicates that these dilute solutions have lower DDA content and a less structured hydrogen-bonding network, which may increase the availability of free water molecules and facilitate side reactions—ultimately compromising electrochemical stability.

The coulombic efficiency (CE), η = (discharge time/charge time) × 100, calculated from the GCD results (Fig. 2g–i), shows a direct correlation with the CV analysis. At 1 m, the CE is generally low, indicating significant energy losses during charge/discharge cycles (Fig. 2g). This inefficiency is further supported by the asymmetric shape of the discharge curves in both the CV (Fig. S6a) and GCD results (Fig. S8), suggesting the occurrence of parasitic reactions. These findings highlight the limitations of dilute electrolytes in maintaining efficient and reversible charge storage processes. Raman spectroscopy provides additional insight into this behavior. In dilute electrolytes, the weaker hydrogen-bonding networks, which are evidenced by a lower DDA structure, may contribute to increased side reactions and reduced CE. In contrast, at higher concentrations (5 m and 10 m, as shown in Fig. S9 and S10), the stronger solvation structures, with higher DDA content,

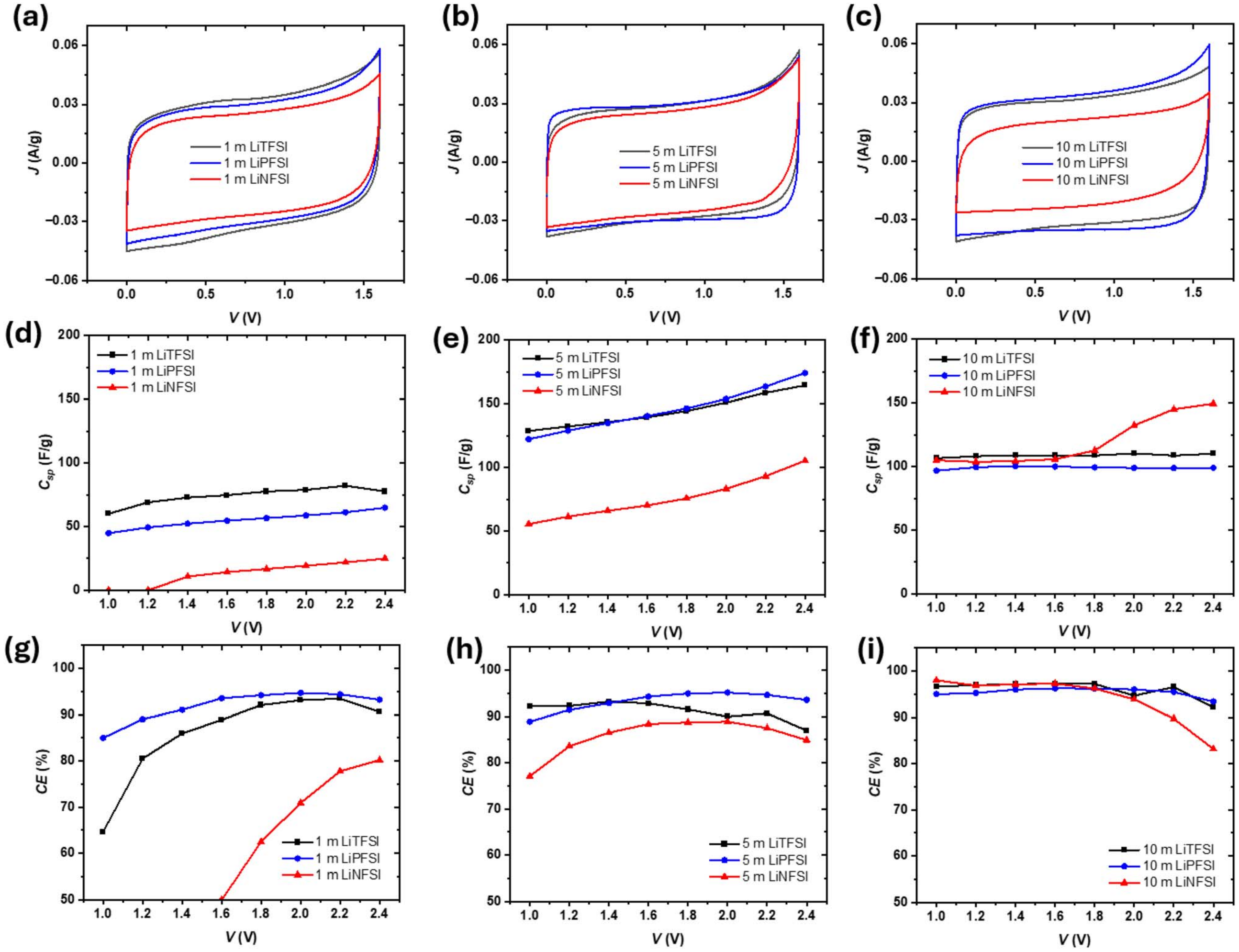

Fig. 2 Electrochemical performance of nanoporous activated carbon using a symmetric two-electrode coin-cell configuration with LiTFSI, LiPFSI, and LiNFSI. CV responses recorded for (a) 1 m, (b) 5 m, and (c) 10 m concentrations at a scan rate of 1 mV s^{-1}; calculated capacitance from GCD measurements of (d) 1 m, (e) 5 m, and (f) 10 m at a current density of 1 A g^{-1} across different voltage ranges; calculated coulombic efficiencies at (g) 1 m, (h) 5 m, and (i) 10 m concentrations, respectively. J, V, C_{sp}, CE indicate current density, voltage, specific capacitance, and coulombic efficiency, respectively.

correlate with enhanced electrochemical stability and improved CE (Fig. 2h and i), consistent with earlier observations.

At a high concentration of 10 m, the electrochemical behavior of LiTFSI and LiPFSI differs from that at lower concentrations. The capacitance values remain nearly constant despite increasing voltage, in line with the ESW observed in the CV data. This stability suggests effective suppression of electrolyte decomposition and electrode degradation, likely due to modified solvation structures that reduce the number of free solvent molecules, as confirmed by Raman spectroscopy (Fig. 1). The high CE observed at 10 m further reflects the minimal side reactions and more efficient charge storage processes under these conditions. In contrast, LiNFSI exhibits markedly different behavior at high concentrations. GCD results reveal a significant drop in charge/discharge efficiency, which is attributed to the high viscosity of the electrolyte, impairing ion transport and increases internal resistance, as is evident from the increased ohmic drop and decreased capacitance (Fig. S10). Additionally, the bulky $NFSI^-$ anion, which is non-spherical and conformationally flexible, possesses a larger effective spatial extent than $TFSI^-$ and $PFSI^-$. For comparison, structural analyzes of ionic liquids have shown that the effective longer molecular dimension of the $TFSI^-$ anion is approximately 0.79 nm,[57] a value already comparable to the dominant pore size (~0.87 nm) of the YEC-8A activated carbon used in this study. The longer perfluoroalkyl chain of $NFSI^-$, combined with strong ion pairing and aggregation at high concentrations, is therefore expected to further increase the effective size of the charge-carrying species, limiting access to narrow micropores and contributing to the observed capacitance loss (see further discussion below). Similarly, X-ray scattering data suggests that the characteristic *d*-spacing of the aggregates formed by these ions ranges from 0.7 to 1.1 nm, as the anion size increases.[48] It is therefore possible that the optimal capacitance of $PFSI^-$ anion reflects the match between the modal average pore size and the anion size. The presence of residual water may trigger parasitic faradaic reactions such as water electrolysis. This behavior is consistent with the CV data, which show a sharp increase in capacitance beyond 1.8 V, indicating faradaic contributions rather than purely capacitive charging. These factors collectively limit the practical application of LiNFSI in high-voltage energy storage systems. Long-term cycling stability results (Fig. S11) further reinforce these findings.

To further validate these findings, electrochemical impedance spectroscopy (EIS) was performed. The Nyquist (Fig. S12) and Bode plots (Fig. S13) obtained from EIS are used to provide qualitative insights into the accessibility within the porous electrode structure and elucidate ion transport behavior at the electrode–electrolyte interface as a function of frequency.[58] In the Nyquist plot, the high-frequency region reveals that at 1 m concentration (Fig. S12a), LiTFSI exhibits a lower equivalent series resistance (ESR, real-axis intercept) and charge transfer resistance (semicircle diameter) compared to LiPFSI. However, this trend reverses at higher concentrations: at 5 m (Fig. S12b) and 10 m (Fig. S12c), LiPFSI demonstrates lower ESR and charge transfer resistances compared to LiTFSI. These trends are consistent with the CV and GCD results, reinforcing the observed improvements in electrochemical performance at higher concentrations. Notably, LiNFSI consistently shows the highest ESR and charge transfer resistance across all concentrations, reflecting its sluggish ion transport properties. The Bode plot (Fig. S13) provides additional insights into the frequency dependent capacitive behavior of the electrolytes. As the frequency decreases, the phase angle shifts negatively, with ideal supercapacitor behavior approaching $-90°$.[59] At 5 m, LiTFSI reaches a phase angle of $-45°$ more rapidly (at a higher frequency) than LiPFSI, suggesting more efficient ion transport and faster double-layer formation. However, this trend reverses at 10 m, where LiPFSI surpasses LiTFSI, indicating a shift in ion transport dynamics.[60] The frequency corresponding to the $-45°$ phase angle serves as a key indicator of capacitive performance, highlighting the balance between surface and pore-level ion transport.[59] The observed reversal in the phase angle trend at 10 m suggests that the reduced solvation of LiPFSI facilitates deeper ion penetration into the micropores, enhancing diffusion-controlled charge storage. This observation aligns with previous reports in ionic liquid-based systems,[61,62] reinforcing the conclusion that capacitance and overall electrochemical performance are closely governed by the pore characteristics of the electrode and the hydration structure of the WIS electrolyte.

While the two-electrode setup effectively captures overall energy storage behaviour, it is limited in isolating the intrinsic electrochemical characteristics of individual electrodes. To address this, a three-electrode Swagelok-type cell was also employed in this study, allowing for a more accurate and detailed comparison of electrode behaviour. This configuration enables clearer differentiation of the charge storage mechanisms and more precise evaluation of electrolyte-dependent performance differences.

Fig. 3a–c presents the CV results for electrolyte solutions containing different anions, measured across varying concentrations. The CV experiments were conducted at a low scan rate of 1 mV s^{-1} to accurately detect faradaic reactions such as electrolyte decomposition. For these experiments, the measurements were performed by sweeping the voltage from 0 V (*vs.* AgQRE) in both positive and negative directions. The results showed that all electrolytes, except for 10 m LiNFSI, exhibited a characteristic rectangular CV shape indicative of EDLC behaviour across all tested concentrations. However, as the scan rate increased (Fig. S13 and S14 at 10 mV s^{-1} and 100 mV s^{-1}, respectively), the rectangular CV shape gradually distorted. This phenomenon occurs because, at higher scan rates, the ability of ions within the electrolyte to reach the electrode surface becomes increasingly limited at higher currents. In other words, at high scan rates, ions do not have sufficient time to migrate and interact with the electrode surface, leading to the increasing resistance observed in the CV. In a typical EDLC system, the capacitance tends to decrease at high scan rates, as ion transport becomes the rate-limiting factor. However, for 10 m LiNFSI, the opposite trend was observed. At a high scan rate of 100 mV s^{-1} (Fig. S15), the CV retained a nearly rectangular shape and exhibited the highest capacitance. Conversely, as the scan rate decreased to 1 mV s^{-1} (Fig. 3c), the CV curve transitioned to almost linear *I*–*V* curve, with a sharp decline in capacitance (specific capacitance values calculated from CV areas can be found in Fig. S16). This anomalous behavior can be attributed to the high viscosity and low ionic conductivity of the 10 m LiNFSI electrolyte (Fig. S1). At high scan rates, the dominant charge storage mechanism appears to be limited to interfacial ion rearrangement near the outer surface of the nanoporous electrode. In such cases, ions do not have time to penetrate far into electrode pores, but fast rearrangement of ions at the electrode/electrolyte interface can still support capacitive behaviour. Interestingly, this surface-dominated charge storage remains efficient for 10 m LiNFSI at high scan rates, despite the system's slow ion mobility. At low scan rates, more time is available for ions to access the internal porous network, which ideally should lead to higher capacitance. However, in the case of 10 m LiNFSI, this deeper pore accessibility is severely limited. The large effective size of the $NFSI^-$ anion, together with the high viscosity of electrolyte, restricts ion mobility and prevents effective ion transport into sub-nanometre pores. For comparison, the dominant pore size of the YEC-8A activated carbon (0.87 nm) is slightly larger than the effective molecular dimension of the $TFSI^-$ anion ($\sim$0.79 nm).[57] The longer fluorinated chain of $NFSI^-$, combined with strong ion pairing and aggregation at high concentration, is therefore expected to further increase the effective size of the charge-carrying species, making ion entry into narrow micropores sterically hindered and energetically unfavourable. Under these conditions, crowding, ion layering, and electrostatic confinement effects dominate, leading to limited pore utilization and suppressed capacitance despite the low scan rate.

This behaviour aligns with prior observations in ionic liquids and highly concentrated electrolytes, where interfacial ion dynamics dominate at high scan rates, enabling efficient charge storage near the electrode surface. At lower scan rates, however, charge storage increasingly depends on ion transport into the internal porous structure of the electrode, which

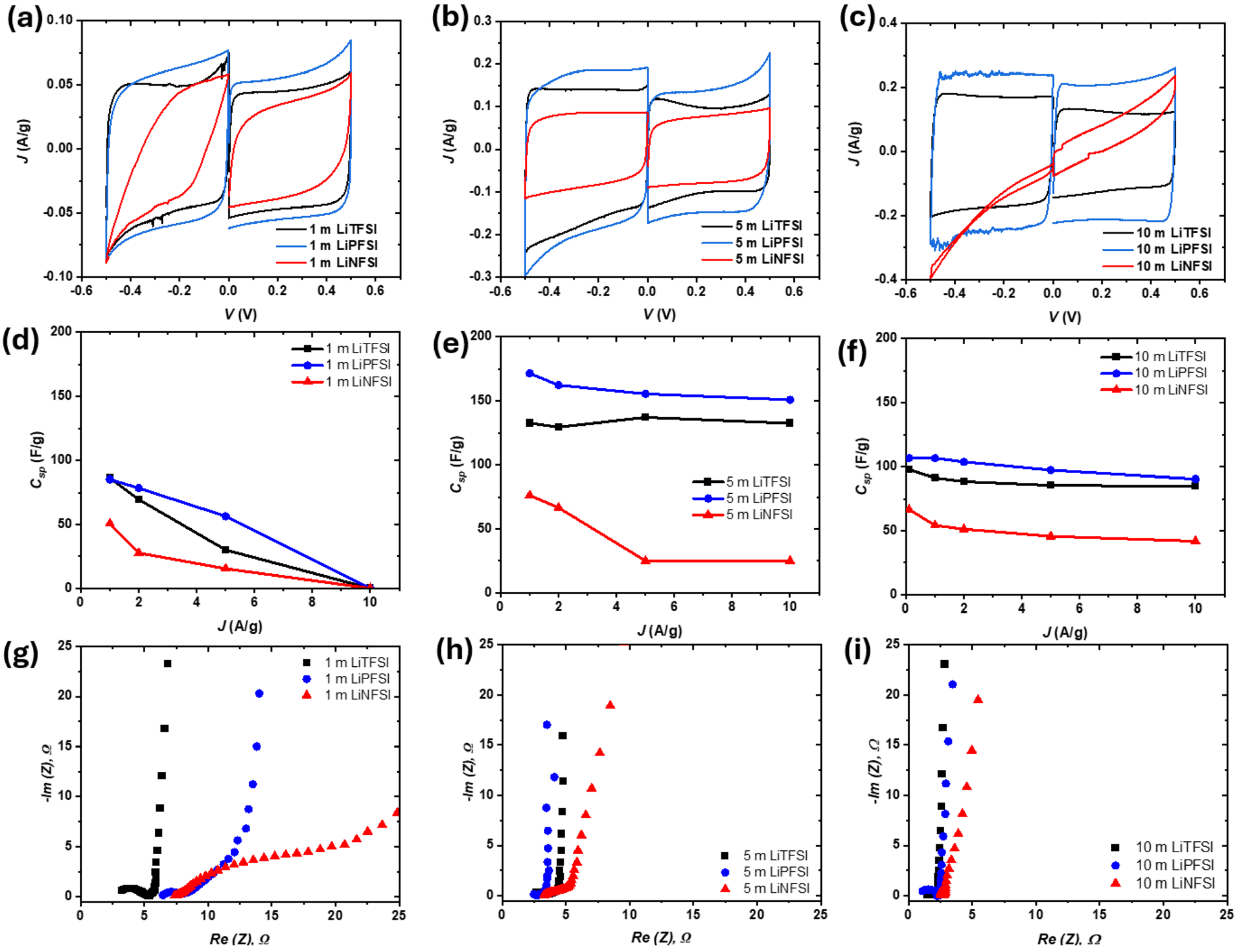

Fig. 3 Electrochemical performance of nanoporous activated carbon using a three-electrode Swagelok cell configuration with LiTFSI, LiPFSI, and LiNFSI. CV profiles of (a) 1 m, (b) 5 m, and (c) 10 m concentrations at a scan rate of 1 mV s^{-1}; calculated specific capacitance from GCD profiles of (d) 1 m, (e) 5 m, and (f) 10 m concentrations at the positively polarized electrode with a current density of 1 A g^{-1}; and Nyquist plots of (g) 1 m, (h) 5 m, and (i) 10 m concentrations.

becomes rate-limiting in systems with sluggish ionic mobility. In such cases, especially when pore sizes approach the dimensions of solvated ions, charge storage is further hindered by confinement effects, including ion layering, crowding, and overscreening at electrified interfaces.[63] Thus, for 10 m LiNFSI, the charge storage mechanism transitions from surface-limited to diffusion-limited behaviour as scan rate decreases, underscoring the importance of both ion properties and pore accessibility in highly concentrated system.

To further elucidate the impact of pore architecture under conditions where internal pore transport dominates, we compared two carbon electrodes: YEC-8A (average pore size: ∼0.87 nm) and YP-50F (1.1–1.8 nm).[64,65] Fig. S16 shows the CV measurements collected at a scan rate of 1 mV s^{-1} for various LiNFSI concentrations using a 3-electrode configuration. While a direct comparison of specific capacitance between different activated carbons is complicated due to variations in morphology and surface functionality, we can still assess the influence of pore size, particularly when using longer chain ions ($NFSI^-$). At 1 m and 5 m (Fig. S17a and b), YP-50F exhibited slightly higher capacitance than YEC-8A, likely due to its broader pore structure enabling greater ion accessibility (specific capacitance values calculated from CV areas can be found in Fig. S18). Despite these differences, at these concentrations both carbon electrodes performed without significant transport limitations. However, at a 10 m concentration, the performance diverged clearly. As previously discussed, YEC-8A showed severely distorted CVs and diminished capacitance, indicative of hindered ion transport. In contrast, YP-50F maintained a more rectangular CV shape and higher specific capacitance (Fig. S17c and S18), suggesting that its wider pores mitigated the steric and transport challenges posed by bulky $NFSI^-$ anions. This comparison emphasizes that ion transport is influenced not only by electrolyte properties but also by the match between pore size and ion dimensions. It is important to note, however, that larger pores are not universally better, *e.g.*, prior studies suggested optimal double-layer capacitance occurs near ∼0.85 nm in aqueous systems.[66] Nonetheless, under the extreme conditions of 10 m LiNFSI, *i.e.*, high viscosity, low mobility, and ion clustering, such narrow pores become largely inaccessible. These findings highlight the need for co-optimization of electrolyte chemistry and pore architecture to achieve efficient charge storage under high concentration conditions.

To further validate the influence of electrolyte composition on charge storage behaviour across a range of concentrations, we calculated specific capacitance values from the GCD curves recorded at current densities from 0.1 A g^{-1} to 10 A g^{-1} for the positive electrode (0–0.5 V *vs.* AgQRE) and are presented in Fig. 3d–f. These values corroborate CV trends, following the order LiPFSI > LiTFSI > LiNFSI, with a maximum at 5 m. While GCD-based capacitance values are lower than those from CV (Fig. S19), this discrepancy is expected due to contributions from parasitic currents at voltage extremes, which are more prominent in CV due to its potentiostatic nature.[56,67] The capacitance values calculated for the negative electrode (−0.5 to 0 V *vs.* AgQRE) are also shown in Fig. S19. Although Li^+ adsorption occurs predominantly at the negative electrode, the identity of the counterion significantly affects the overall charge screening environment. In highly concentrated systems, such as 10 m LiNFSI, interfacial ion organization is strongly modulated by ion–ion correlations. According to the Kornyshev model and related work on ionic liquids, phenomena such as "over-screening" or "crowding" can occur at the electrode interface, leading to anion-induced changes in double-layer structure and capacitance. These effects are particularly relevant under high current densities, where ion layering and local structuring play an important role in determining device performance.[68–70] Fig. 3g–i presents the Nyquist plots measured at 0 V (*vs.* AgQRE). Notably, all three Li-based electrolyte solutions containing different anions exhibit the steepest slopes at a concentration of 5 m, which can be interpreted as the most ideal EDLC behavior (slope closest to vertical). The observed decrease in slope at low frequencies, despite the measurement being at 0 V where faradaic reactions are not expected, may arise from other interfacial processes such as ion diffusion limitations or subtle surface adsorption phenomena at the electrode/electrolyte interface.[71] Such variations in slope may also be influenced by the porous structure of the electrode, interfacial resistance, and ion diffusion processes.

To further investigate the retention of electrolyte species on the electrode surface after electrochemical cycling, post-mortem Raman spectroscopy and X-ray diffraction (XRD) analyses were conducted. Raman spectra indicate that LiTFSI and LiPFSI were almost undetected on the carbon surface after electrochemical experiments (Fig. S20), suggesting their efficient desorption and removal from the electrode. In contrast, LiNFSI could still be detected, even at a 5 m concentration, with an increasing Raman signal at higher concentrations. XRD analysis further supports these findings, showing the presence of residual LiNFSI species on the electrode surface post-cycling, while no crystalline phases related to LiTFSI or LiPFSI were observed (Fig. S21). Although some retention may result from the absence of a washing step, the consistent difference across identically treated samples suggests that LiNFSI exhibits a stronger affinity for the carbon surface as also evidenced by its lower contact angle and improved wettability. While EIS techniques are undoubtedly a powerful tool for elucidating the reaction mechanisms of supercapacitors, in highly concentrated electrolytes, diffusion processes within the electrolyte may predominantly determine the overall behavior, even if redox-active species capable of inducing faradaic reactions are present. Moreover, the behavior of ions adsorbed on the electrode surface often remains relatively stable across much of the frequency spectrum, with noticeable changes typically occurring only in the very low-frequency region.[72] Therefore, to further investigate the extent to which the electrolyte penetrates the nanopores of electrode, we conducted additional NMR analysis. This approach allowed us to assess whether the electrolyte effectively infiltrates the micropores of the electrode, or if ion transport is restricted at specific pore sizes, thereby providing a more precise interpretation of the low-frequency behavior observed in the EIS analysis.

To gain insight into the wetting of the carbon surface, magic-angle spinning (MAS) NMR experiments were performed on carbon soaked with LiPFSI. Measurements were carried out by soaking a defined mass of YEC-8a carbon (15 mg) with 20 μL of electrolyte within a MAS rotor. The volume of electrolyte used is approximately 1.3 times larger than the pore volume of the carbon sample. The sealed rotor was then spun at 5 kHz and ^1H and ^{19}F MAS NMR spectra were recorded. Fig. 4a shows ^1H MAS NMR spectra of carbon soaked with LiPFSI at concentrations between 1 m and 10 m. In each spectrum, two main resonances are observed. Peaks at higher (more positive) chemical shift values correspond to species in excess electrolyte outside the carbon particles (ex-pore). Peaks at lower chemical shifts (more negative) correspond to species in electrolyte adsorbed within the carbon pores (in-pore). The origin of the shift difference between in-pore and ex-pore environments is magnetic field-induced ring currents associated with the delocalized electrons within the carbon surface.[73,74]

As the concentration increases from 1 m to 10 m, the overall intensity of the spectrum reduces, reflecting the lower water content of the sample. Within each spectrum, the intensity of the ex-pore resonance at ∼4 ppm reduces relative to the intensity of the in-pore resonance at −0.5 ppm. This shows that the water preferentially occupies the in-pore environment. As the total amount of water reduces with increasing concentration, the ex-pore environment is depleted in preference to the in-pore environment. Because the ex-pore resonance overlaps slightly with the in-pore resonance, the intensity of the in-pore resonance also reduces by a small amount with increasing concentration. The magnitude of the ring current shift between the in-pore and ex-pore resonances is approximately 5 ppm, which is consistent with values measured in other studies.[38,75,76] For the 10 m concentration, the ring current shift is slightly reduced due to a small reduction in the chemical shift of the ex-pore resonance. This suggests that hydrogen bonding in the ex-pore water is reduced, which is consistent with the relatively low concentration of water remaining in the ex-pore environment which will, on average, see a more LiPFSI-rich environment. Deconvolutions of the 1 m and 10 m spectra (Fig. S22) show

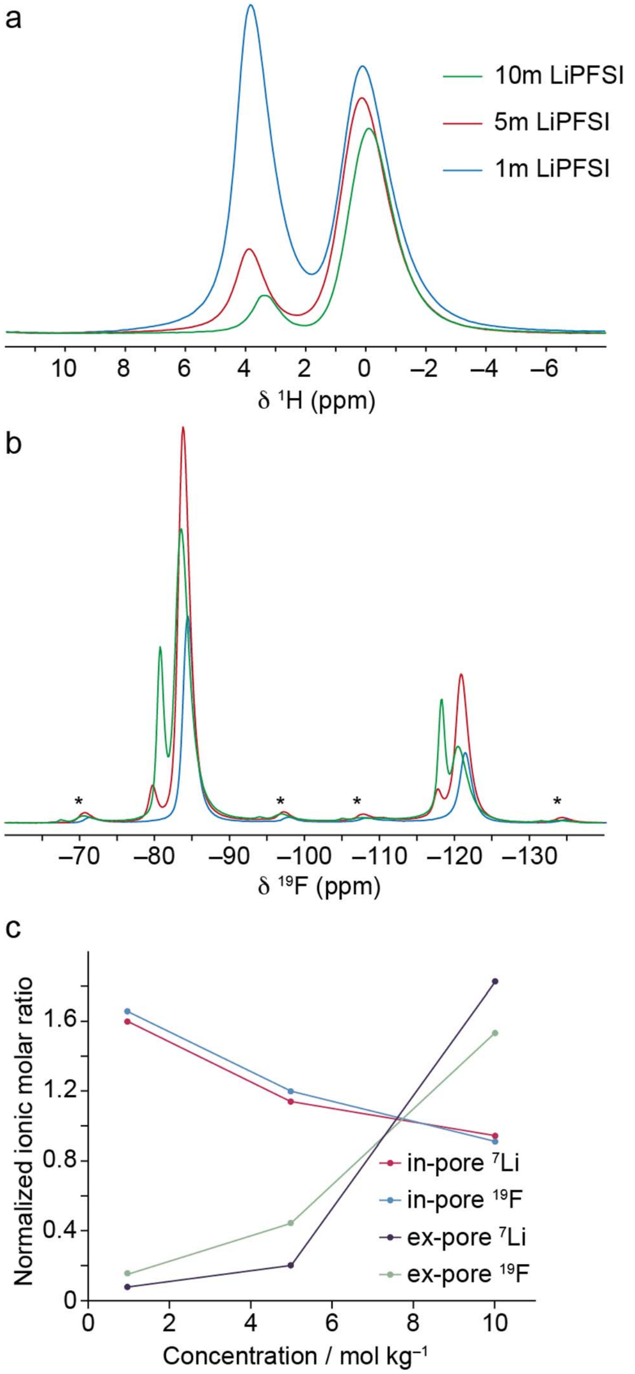

Fig. 4 (a) ^{1}H and (b) ^{19}F MAS NMR spectra of YEC-8A (13 mg) soaked with 20 μL of LiPFSI electrolytes at different concentrations. (c) Normalized in-pore and ex-pore ionic molar ratios determined from deconvolution of the MAS NMR spectra.

evidence of multiple in-pore environments which likely reflects a range of pore environments present in the disordered carbon structure.

Fig. 4b shows ^{19}F MAS NMR spectra of same samples. In each spectrum, two sets of resonances are observed corresponding to the CF_2 (−118–−121 ppm) and CF_3 (−80–−85 ppm) groups in the PFSI side chains. In these spectra, the overall intensity follows the opposite trend to the ^{1}H spectra, reflecting the increasing PFSI content of the sample as the electrolyte concentration increases. For the 1 m concentration, only in-pore resonances are observed at −85 and −121 ppm, showing that the $PFSI^-$ ions preferentially occupy the in-pore environment and a negligible proportion remain in the ex-pore environment. This indicates that the ex-pore H_2O observed in the ^{1}H MAS NMR spectrum is essentially free water that is depleted of LiPFSI. As the electrolyte concentration increases, ex-pore resonances at −80 and −118 ppm emerge and increase in intensity. This suggests that the emergence of the ex-pore resonance arises from pore saturation, where, above a certain loading and concentration, there is no space remaining in the in-pore environment and the LiPFSI is forced to occupy the ex-pore environment. This trend is also mirrored by the ^{7}Li MAS NMR spectra of the same samples (Fig. S22), which shows that the partitioning of the Li cations between the in-pore and ex-pore environments broadly follows that of the PFSI anions. In the 5 m spectrum, the intensities of the in-pore resonances appear higher than in the 10 m spectrum; however, deconvolutions reveal the in-pore ion populations for both concentrations are very similar (Table S2), further evidencing saturation of the in-pore environment. Deconvolutions also enable the local ion : water molar ratios within the in-pore and ex-pore environments to be determined (Table S2).[38] These can be normalized by the ionic molar ratios of the neat solutions, where a value below 1 shows that the local concentration is reduced relative to the neat solution, and a value above 1 shows that the local concentration is increased relative to the neat solution. As shown in Fig. 4c, the normalized in-pore ionic ratio reduces with increasing concentration, while the normalized ex-pore concentration increases with increasing concentration. The crossing point appears to be at a concentration of approximately 7 m, which corresponds to where the H_2O and LiPFSI would be expected to be equally distributed across the system.

Overall, the NMR results show that LiPFSI preferentially occupies the in-pore environment, and only occupies the ex-pore environment when the pores become saturated with high-concentration loadings. This is broadly in line with the HOPG contact angle measurements which demonstrate the high affinity of LiPFSI for the carbon surface, although the pronounced differences in the in-pore electrolyte composition viewed by NMR highlight the subtleties of the relative affinities of LiPFSI and H_2O for the carbon surface in a way which is not evident from the bulk contact angle measurement. Indeed, the carbon-LiPFSI system exhibits a degree of hydrophobicity which appears to depend on the bulk electrolyte concentration. At 1 m concentration when all of the LiPFSI is inside the pores, it can accommodate a smaller fraction of the H_2O than when in the bulk, resulting in some H_2O residing outside the pores. At 10 m concentration, almost all of the H_2O is accommodated inside the pores, although the total amount of H_2O present here is much lower than in the 1 m sample. In the 5 m sample, the in-pore environment contains the highest combined amount of LiPFSI and H_2O of the samples studied. It should be noted that in a functioning capacitor, the electrolyte is present in excess relative to the carbon, so there will be ex-pore H_2O and LiPFSI in all cases. However, the in-pore electrolyte composition in the absence of an applied potential is expected to be broadly comparable to the observations made here. This may indicate that the maximum capacitance observed at ∼5 m concentration corresponds to where the in-pore electrolyte has an optimum balance between the number of ions present to store charge, and the amount of H_2O present to facilitate movement of the ions through the porous network during charging.

These results provide practical guidelines for designing high-voltage aqueous supercapacitors: selecting mid-concentration electrolytes and matching them with suitable carbon pore sizes optimizes ion transport and charge storage, highlighting the importance of co-designing electrolyte chemistry and electrode architecture.

4. Conclusion

This work demonstrates that the electrochemical performance of highly concentrated aqueous electrolytes is influenced not simply by bulk solvation characteristics, but by ionic distribution into nanoporous carbon and by interfacial ion–surface interactions under applied potential. While Raman spectroscopy provides insight into hydrogen-bonding and ion coordination in bulk solution, solid-state NMR reveals that the decisive factor is the in-pore electrolyte composition, *i.e.*, the ion to solvent ratio and how it evolves with concentration. LiPFSI offers the optimal trade-off between ion mobility and effective adsorption at the electrode interface, slightly outperforming the smaller LiTFSI and the bulkier, more viscous LiNFSI. The intermediate size of the PFSI anion enables sufficient coordination and interaction with the carbon surface while avoiding the limited transport and pore exclusion observed with LiNFSI. NMR results show that LiPFSI preferentially occupies the in-pore environment and reaches saturation near 5 m, indicating that optimal charge storage occurs when the ion concentration and solvent content are balanced within the confined carbon environment, which is close to the experimentally determined conductivity maximum. It is likely that similar factors dictate the capacitance and conductivity dependence on concentration and the latter may, therefore, be a good predictor for the former, at least for certain types of electrolyte.

These findings highlight that carbon pore accessibility, alongside ion size and solvation behavior, is a critical factor in determining performance. Future design of electrolytes for supercapacitor applications should therefore consider not only bulk physicochemical properties, but also how ions interact with and distribute within the nanoporous electrode structure. This integrated understanding is essential for advancing high-concentration aqueous electrolytes tailored specifically for next generation supercapacitor technologies.

Author contributions

Imgon Hwang: conceptualization, methodology, investigation, validation, formal analysis, Mantas Leketas: conceptualization, investigation, formal analysis, Sittipong Kaewmorakot: methodology, data curation, Ryan Bragg: methodology, John M. Griffin: methodology, funding acquisition, Robert A. W. Dryfe: conceptualization, validation, supervision, funding acquisition. I. H. and R. A. W. D. wrote the manuscript with input from the other authors. All authors contributed to the discussion and interpretation of the data presented in the work.

Conflicts of interest

The authors declare that they have no known competing financial interests or personal relationships that could have appeared to influence the work reported in this paper.

Data availability

Data will be made available upon reasonable request.

Supplementary information (SI): data on bulk solution properties, contact angles of the electrolytes, further Raman, XRD and NMR data, along with more detailed electrochemical data. See DOI: https://doi.org/10.1039/d5ta09457g.

Acknowledgements

The authors would like to acknowledge the EPSRC (EP/V049925/1 and EP/V05001X/1) for financial support.

References

1 P. Simon and Y. Gogotsi, Perspectives for electrochemical capacitors and related devices, *Nat. Mater.*, 2020, **19**, 1151.

2 M. Salanne, B. Rotenberg, K. Naoi, K. Kaneko, P. L. Taberna, C. P. Grey, B. Dunn and P. Simon, Efficient storage mechanisms for building better supercapacitors, *Nat. Energy*, 2016, **1**, 1.

3 M. R. Lukatskaya, B. Dunn and Y. Gogotsi, Multidimensional materials and device architectures for future hybrid energy storage, *Nat. Commun.*, 2016, **7**, 1.

4 F. Beguin, V. Pressure, A. Balducci and E. Frackowiak, Carbons and electrolytes for advanced supercapacitors, *Adv. Mater.*, 2014, **26**, 2219.

5 C. Zhong, Y. Deng, W. Hu, J. Qiao, L. Zhang and J. Zhang, A review of electrolyte materials and compositions for electrochemical supercapacitors, *Chem. Soc. Rev.*, 2015, **44**, 7484.

6 D. R. MacFarlane, N. Tachikawa, M. Forsyth, J. M. Pringle, P. C. Howlett, G. D. Elliott, J. H. Davis Jr, M. Watanabe, P. Simon and C. A. Angell, Energy applications of ionic liquids, *Energy Environ. Sci.*, 2014, **7**, 232.

7 Z. Li, S. Ganapathy, Y. Xu, Z. Zhou, M. Sarilar and M. Wagemaker, Mechanistic insight into the electrochemical performance of Zn/VO_2 batteries with an aqueous ZnSO4 electrolyte, *Adv. Energy Mater.*, 2019, **9**, 1900237.

8 J. Xie, Z. Liang and Y. C. Lu, Molecular crowding electrolyte for high-voltage aqueous batteries, *Nat. Mater.*, 2020, **19**, 1006.

9 C. Zhao and W. Zheng, A review for aqueous electrochemical supercapacitors, *Front. Energy Res.*, 2015, **3**, 23.

10 J. Yu, C. Mu, X. Qin, C. Shen, B. Yan, H. Xue and H. Pang, Development of high-voltage aqueous electrochemical energy storage devices, *Adv. Mater. Interfaces*, 2017, **4**, 1700279.

11 L. Suo, O. Borodin, T. Gao, M. Olguin, J. Ho, X. Fan, C. Luo, C. Wang and K. Xu, "Water-in-salt" electrolyte enables high-voltage aqueous lithium-ion chemistries, *Science*, 2015, **350**, 938.

12 Y. Yamada, K. Usui, K. Sodeyama, S. Ko, Y. Tateyama and A. Yamada, Hydrate-melt electrolytes for high-energy-density aqueous batteries, *Nat. Energy*, 2016, **1**, 16129.

13 R.-S. Kühnel, D. Reber and C. Battaglia, A high-voltage aqueous electrolyte for sodium-ion batteries, *ACS Energy Lett.*, 2017, **2**, 2005.

14 L. Suo, O. Borodin, W. Sun, X. Fan, C. Yang, F. Wang, T. Gao, Z. Ma, M. Schröder, A. von Cresce, S. Russell, M. Armand, A. Angell, K. Xu and C. Wang, Advanced high-voltage aqueous lithium-ion battery enabled by "water-in-bisalt" electrolyte, *Angew. Chem., Int. Ed.*, 2016, **55**, 7136.

15 L. Suo, F. Han, X. Fan, H. Liu, K. Xu and C. Wang, "Water-in-salt" electrolytes enable green and safe Li-ion batteries for large scale electric energy storage applications, *J. Mater. Chem. A*, 2016, **4**, 6639.

16 C. Yang, J. Chen, T. Qing, X. Fan, W. Sun, A. von Cresce, M. S. Ding, O. Borodin, J. Vatamanu, M. Schröder, N. Eidson, C. Wang and K. Xu, 4.0 V aqueous Li-ion batteries, *Joule*, 2017, **1**, 122.

17 F. Wang, Y. Lin, L. Suo, X. Fan, T. Gao, C. Yang, F. Han, Y. Qi, K. Xu and C. Wang, Stabilizing high voltage $LiCoO_2$ cathode in aqueous electrolyte with interphase-forming additive, *Energy Environ. Sci.*, 2016, **9**, 3666.

18 M. Amiri and D. Belanger, Physicochemical and electrochemical properties of water-in-salt electrolytes, *ChemSusChem*, 2021, **14**, 2487.

19 D. Reber, R.-S. Kühnel and C. Battaglia, Suppressing crystallization of water-in-salt electrolytes by asymmetric anions enables low-temperature operation of high-voltage aqueous batteries, *ACS Mater. Lett.*, 2019, **1**, 44.

20 N. Zhang, F. Cheng, J. Liu, L. Wang, X. Long, X. Liu, F. Li and J. Chen, Rechargeable aqueous zinc-manganese dioxide batteries with high energy and power densities, *Nat. Commun.*, 2017, **8**, 405.

21 F. Wang, O. Borodin, T. Gao, X. Fan, W. Sun, F. Han, A. Faraone, J. A. Dura, K. Xu and C. Wang, Highly reversible zinc metal anode for aqueous batteries, *Nat. Mater.*, 2018, **17**, 543.

22 T. Guo, D. Zhou, L. Pang, S. Sun, T. Zhou and J. Su, Perspectives on working voltage of aqueous supercapacitors, *Small*, 2022, **18**, 2106360.

23 A. Bunpheng, P. Chavalekvirat, K. Tangthana-umrung, V. Deerattrakul, K. Nueangnoraj, W. Hirunpinyopas and P. Iamprasertkun, A comprehensive study of affordable "water-in-salt" electrolytes and their properties, *Green Chem. Eng.*, 2025, **6**, 126.

24 K. Kwak, J. Jeon, S. Chun and M. Cho, Ion networks in water-based Li-ion battery electrolytes, *Acc. Chem. Res.*, 2025, **58**, 199.

25 L. Trojanowski, X. Lyu, S.-C. Lee, S. Seifert, Z. Y and T. Li, molecular origin of nanoscale anion ordering of LiTFSI electrolytes revealed through SAXS/WAXS and molecular dynamics simulations, *ACS Energy Lett.*, 2025, **10**, 696.

26 T. K. Kumaresan, A. B. Ikhe, W. Park, S. J. Prabakar, H. Noh, J. Seo, Y. Lee, K. Sohn, J. Kwak and M. Pyo, Highly concentrated asymmetric KTFSI for aqueous potassium ion batteries, *Adv. Energy Mater.*, 2025, **11**, 2402011.

27 G. Vardhini, P. S. Dillp, S. A. Kumar, S. Suriyakumar, M. Hariharan and M. M. Shaijumon, Polyimide-based aqueous potassium energy storage systems using concentrated WiSE electrolyte, *ACS Appl. Mater. Interfaces*, 2024, **16**, 48782.

28 N. Singh and H. K. Kashyap, Are NaTFSI and NaFSI salt-based water-in-salt electrolytes structurally similar or different?, *J. Phys. Chem. B*, 2024, **128**, 7615.

29 P. Wrobel, P. Kubisiak and A. Eilmes, Ab initio molecular dynamics simulations of aqueous LiTFSI solutions-structure, hydrogen bonding, and IR spectra, *J. Phys. Chem. B*, 2024, **128**, 1001.

30 Y. Guo, M. W. Terban, I. Moudrakovski, A. Münchinger, R. E. Dinnebier, J. Popovic and J. Maier, Ion transport in semi-solid in-salt electrolytes: LiTFSI-H2O as a model system, *J. Mater. Chem. A*, 2023, **11**, 3427.

31 G. Horwitz, C. R. Rodriguez, P. Y. Steinberg, G. Burton and H. R. Corti, Mobility-viscosity decoupling and cation transport in water-in-salt lithium electrolytes, *Electrochim. Acta*, 2020, **359**, 136915.

32 C. Long, L. Miao, D. Zhu, H. Duan, Y. Lv, L. Li, M. Liu and L. Gan, Adapting a kinetics-enhanced carbon nanostructure to Li/Na hybrid water-in-salt electrolyte for high-energy aqueous supercapacitors, *ACS Appl. Energy Mater.*, 2021, **4**, 5727.

33 K. Zhang, J. Sun, L. E, C. Ma, S. Luo, Z. Wu, W. Li and S. Liu, Effects of the pore structure of commercial activated carbon on the electrochemical performance of supercapacitors, *J. Energy Storage*, 2022, **45**, 103457.

34 S. Suh, J. Lee, J. Park and W. Kim, The strong correlations between the performance of a KB supercapacitor and the properties of $NaClO_4$ and LiFSI electrolytes over wide concentration ranges, *Int. J. Energy Res.*, 2022, **46**, 18676.

35 P. Sekar, A. Ramadoss and S. Balasubramaniam, Tailoring potential window of aqueous electrolyte via steric molecular engineering for high voltage supercapacitors, *Appl. Mater. Today*, 2023, **32**, 101845.

36 D. Dong, C.-X. Zhao, X. Zhang and C. Wang, Aqueous electrolyte: From salt in water to water in salt and beyond, *Adv. Mater.*, 2025, **38**, 2418700.

37 I. Hwang, M. Leketas, K. Griffiths, R. J. Bragg, J. M. Griffin and R. A. W. Dryfe, Effect of salt concentration in water-in-salt electrolyte on supercapacitor applications, *ChemElectroChem*, 2024, **11**, e202400099.

38 R. J. Bragg, K. Griffiths, I. Hwang, M. Leketas, K. Polus, V. Presser, R. A. W. Dryfe and J. M. Griffin, Solvation

effects on aqueous ion adsorption and electrosoprtion in carbon micropores, *Carbon*, 2024, **229**, 119531.

39 C. Largeot, C. Portet, J. C hmiola, P.-L. Taberna, Y. Gogotsi and P. Simon, Relation between the ion size and pore size for an electric double-layer capacitor, *J. Am. Chem. Soc.*, 2008, **130**, 2730.

40 A. Cassie, Contact Angles, *Faraday Discuss.*, 1948, **3**, 11.

41 R. N. Wenzel, Resistance of solid surfaces to wetting by water, *Ind. Eng. Chem. Res.*, 1936, **28**, 988.

42 E. Pamete and F. Beguin, Effect of salt concentration in aqueous LiTFSI electrolytes on the performance of carbon-based electrochemical capacitors, *Electrochim. Acta*, 2021, **389**, 138687.

43 D. Massiot, F. Fayon, M. Capron, I. King, S. Le Calve, B. Alonso, J.-O. Durand, B. Bujoli, Z. Gan and G. Hoatson, Modelling one- and two-dimensional solid-state NMR spectra, *Magn. Reson. Chem.*, 2002, **40**, 70.

44 N. S. M. Vieira, P. M. Reis, K. Shimizu, O. A. Cortes, I. M. Marrucho, J. M. M. Araujo, J. M. S. S. Esperanca, J. C. Canongia Lopes, A. B. Pereiro and L. P. N. Rebelo, A thermophysical and structural characterization of ionic liquids with alkyl and perfluoroalkyl side chains, *RSC Adv.*, 2015, **5**, 65337.

45 S. Kaewmorakot, A. A. Papaderakis and R. A. W. Dryfe, Electrowetting on glassy carbon substrates, *Nanoscale Adv.*, 2024, **6**, 5441.

46 Q. Sun, The Raman OH stretching bands of liquid water, *Vib. Spectrosc.*, 2009, **51**, 213.

47 R. Vicentini, R. Venancio, W. Nunes, L. M. Da Silva and H. Zanin, New insights on the sodium water-in-salt electrolyte and carbon electrode interface from electrochemistry and operando Raman studies, *ACS Appl. Mater. Interfaces*, 2021, **13**, 61139.

48 X. Liu, S.-C. Lee, S. Seifer, R. E. Winans, L. Cheng, Z. Y and T. Li, Insight into the nanostructure of “water-in-salt” solutions: A SAXS/WAXS study on imide-based lithium salts aqueous solutions, *Energy Storage Mater.*, 2022, **45**, 696.

49 Y. Sui, A. M. Scida, B. Li, C. Chen, Y. Fu, Y. Fang, A. Greaney, T. M. Osborn Popp, D. Jiang, C. Fang and X. Ji, The influence of ions on the electrochemical stability of aqueous electrolytes, *Angew. Chem., Int. Ed.*, 2024, **63**, e202401555.

50 W. Rudolph and G. Irmer, Raman and Infrared spectroscopic investigation of contact ion pair formation in aqueous cadmium sulfate solutions, *J. Solution Chem.*, 1994, **23**, 663.

51 S. A. Berlinger, V. Kupers, P. J. Dudenas, D. Schinski, L. Flagg, Z. D. Lamberty, B. D. MacCloskey, M. Winter and J. Frechette, Cation valency in water-in-salt electrolytes alters the short- and long-range structure of the electrical double layer, *Proc. Natl. Acad. Sci. U. S. A.*, 2024, **121**, e2404669121.

52 L. Suo, D. Oh, Y. Lin, Z. Zhuo, O. Borodin, T. Gao, F. Wang, A. Kushima, Z. Wang, H.-C. Kim, Y. Qi, W. Yang, F. Pan, J. Li, K. Xu and C. Wang, How solid-electrolyte interphase forms in aqueous electrolytes, *J. Am. Chem. Soc.*, 2017, **139**, 18670.

53 M. Zhang, S. Makono, D. Mochizuki and W. Sugimoto, High-performance hybrid supercapacitors enabled by protected lithium negative electrode and “water-in-salt” electrolyte, *J. Power Sources*, 2018, **396**, 498.

54 M. Zhang, Y. Li and Z. Shen, “Water-in-salt” electrolyte enhanced high voltage aqueous supercapacitor with all-pseudocapacitive metal-oxide electrodes, *J. Power Source*, 2019, **414**, 479.

55 P. M. Biesheuvel, Y. Fu and M. Z. Bazant, Diffuse charge and faradaic reactions in porous electrodes, *Phys. Rev. E*, 2011, **83**, 061507.

56 A. J. Bard and L. R. Faulkner, *Electrochemical Methods: Fundamentals and Applications*, Wiley, New York, 2001.

57 C. Brance, A. Arcovito, E. Cosio, M. Interdonato, G. Sabatino, U. Wanderlingh and G. D'Angelo, Combining Fourier transform infrared and Raman spectroscopies with Gaussian deconvolution: An improved approach for the characterization of emeralds, *J. Raman Spectrosc.*, 2020, **51**, 693.

58 B. A. Mei, O. Munteshari, J. Lau, B. Dunn and L. Pilon, Physical interpretations of Nyquist plots for EDLC electrodes and device, *J. Phys. Chem. C*, 2018, **122**, 194.

59 K. Mahankali, N. K. Thangavel, Y. Ding, S. K. Putatunda and L. M. R. Arava, Interfacial behavior of water-in-salt electrolytes at porous electrodes and its effect on supercapacitor performance, *Electrochim. Acta*, 2019, **326**, 134989.

60 A. Parejo-Tovar and F. Beguin, The $NaClO_4$-water eutectic electrolyte for environmentally friendly electrical double-layer capacitors operating at low temperature, *Energy Storage Mater.*, 2024, **69**, 103387.

61 F. W. Richey, C. Tran, V. Kalra and Y. A. Elabd, Ionic liquid dynamics in nanoporous carbon nanofibers in supercapacitors measured with in operando infrared spectroelectrochemistry, *J. Phys. Chem. C*, 2014, **118**, 21846.

62 F. W. Richey, B. Dyatkin, Y. Gogotsi and Y. A. Elabd, Ion dynamics in porous carbon electrode in supercapacitors using in situ infrared spectroelectrochemistry, *J. Am. Chem. Soc.*, 2013, **135**, 12818.

63 M. V. Fedorov and A. A. Kornyshev, Ionic liquids at electrified interfaces, *Chem. Rev.*, 2014, **114**, 2978.

64 J. Bang, B. Lee, Y. Choi, H. Lee and B. Kim, A study on superior mesoporous activated carbons for ultra power density supercapacitor from biomass precursors, *Int. J. Mol. Sci.*, 2022, **23**, 8537.

65 B. Karamanova, A. Stoyanova, M. Shipochka, S. Veleva and R. Stoyanova, Effect of alkaline-basic electrolytes on the capacitance performance of biomass-derived carbonaceous materials, *Materials*, 2020, **13**, 2941.

66 D. Dong, Y. Zhang, T. Wang, J. Wang, C. E. Romero and W. Pan, Enhancing the pore wettability of coal-based porous carbon as electrode materials for high performance supercapacitors, *Mater. Chem. Phys.*, 2020, **252**, 123381.

67 L. E. Helseth, Comparison of methods for finding the capacitance of a supercapacitor, *J. Energy Storage*, 2021, **35**, 102304.

68 A. A. Kornyshev, Double-layer in ionic liquids: paradigm change?, *J. Phys. Chem. B*, 2007, **111**, 5545.

69 M. Z. Bazant, B. D. Storey and A. A. Kornyshev, Double layer in ionic liquids: overscreening versus crowding, *Phys. Rev. Lett.*, 2011, **106**, 046102.

70 S. Begic, F. Chen, E. Jonsson and M. Forsyth, Overscreening and crowding in electrochemical ionic liquid systems, *Phys. Rev. Mater.*, 2019, **3**, 095801.

71 A. M. P. Sakita, R. D. Noce and R. L. Lavall, Potential-dependent electrochemical impedance spectroscopy as a powerful tool for evaluating supercapacitor electrode performance, *J. Electrochem. Soc.*, 2021, **168**, 080525.

72 A. M. P. Sakita, P. F. R. Ortega, G. G. Silva, R. D. Noce and R. L. Lavall, Unveiling the performance metrics for supercapacitor electrodes with adsorbed redox additives, *Electrochim. Acta*, 2021, **390**, 138803.

73 A. C. Forse, C. Merlet, C. P. Grey and J. M. Griffin, NMR studies of adsorption and diffusion in porous carbonaceous materials, *Prog. Nucl. Magn. Reson. Spectrosc.*, 2021, **124–125**, 57.

74 L. Borchardt, M. Oschartz, S. Paasch, S. Kaskel and E. Brunner, Interaction of electrolyte molecules with carbon materials of well-defined porosity: characterization by solid-state NMR spectroscopy, *Phys. Chem. Chem. Phys.*, 2013, **15**, 15177.

75 I. Hwang, M. Leketas, S. Kaewmorakot, R. J. Bragg, J. M. Griffin and R. A. W. Dryfe, Cation-dependent solvation and charge storage in water-in-salt electrolytes: insights from alkali metal trifluoroacetates, *Electrochim. Acta*, 2025, inpress.

76 D. Lyu, K. Märker, Y. Zhou, E. W. Zhao, A. B. Gunnasdóttir, S. P. Niblett, A. C. Forse and C. P. Grey, *J. Am. Chem. Soc.*, 2024, **146**, 9897.